applied sciences

MDPI

Article

Analysis and Design of Protection Device for Anchor Cable Pull-Out in High-Stress Roadways

Fuxin Guo *, Min Tu * and Jiaxin Dang

School of Mining Engineering, Anhui University of Science and Technology, Huainan 232001, China; dangjiaxin3@163.com

* Correspondence: austfuxin@163.com (F.G.); mtu@aust.edu.cn (M.T.); Tel.: +86-0554-6631221 (F.G. & M.T.)

Abstract: In regions with high-stress roadway stress, anchor cables frequently experience damage, leading to risky pull-outs and ejections. This study aimed to determine the dynamics of such incidents, refine protective devices, and validate their efficacy in enhancing safety. Drawing from an ejection accident in the 1632 (3) roadway of Pan San Mine, a combination of laboratory experiments, theoretical analysis, simulations, and field applications was utilized. The kinetic energy and speed of cable ejections were determined from single-axis tension test data. Based on these insights, a spring-based protection device was conceptualized. Subsequent experiments and simulations evaluated the energy absorption and deformation characteristics of these devices with different diameters. The results included the following: A cable, during ejection, moved at 48 m/s. Spring protective devices of 4 mm can absorb more energy than the 5 mm, but the anti-ejection effect is poor respectively. Increasing the device diameter improved its performance, especially in controlling spring deformation rate and preventing cable lock-ups. This devised protection mechanism showed promising results when implemented in the 1511 (1) roadway of Zhangji Mine.

Keywords: anchor cable; ejection; strain energy; protective devices of spring

check for updates

Citation: Guo, F.; Tu, M.; Dang, J. Analysis and Design of Protection Device for Anchor Cable Pull-Out in High-Stress Roadways. *Appl. Sci.* **2023**, *13*, 12023. https://doi.org/10.3390/app132112023

Academic Editor: Hai Pu

Received: 22 September 2023
Revised: 25 October 2023
Accepted: 30 October 2023
Published: 3 November 2023

Copyright: © 2023 by the authors. Licensee MDPI, Basel, Switzerland. This article is an open access article distributed under the terms and conditions of the Creative Commons Attribution (CC BY) license (https://creativecommons.org/licenses/by/4.0/).

1. Introduction

As coal resources are exploited deeply in China, the surrounding rock of roadways is subjected to "three high and one disturbance" complex stress conditions, and anchor wire breaking and ejection becomes increasingly severe.

Anchor wire breaking and ejection kinetic energy and its prevention have been extensively investigated by Chinese and foreign scholars from the perspective of the mechanical state of anchors. Gu [1] and Zheng et al. [2] proposed a formula for the wire breaking and ejection speed of anchors and discussed a protection scheme for anchor wire breaking and ejection. He [3] established a grouting anchor cable model with a composite breaking effect that could improve the bearing capacity of surrounding rocks. Yang et al. [4] developed a set of anchor double-shear test systems and studied the mechanical properties of anchors from the aspects of mortar block specimen, anchorage mode, and prestress. Deng [5] believed that anchor shear via steel strips was the cause of anchor tail breaking, and the fracture of the anchor body resulted from the composite anchor damage induced by roof separation and dislocation. Niu et al. [6–8], Wang et al. [8], and Liu et al. [9] proposed the use of anchor pre-tightening force to improve the stiffness of rock strata and adjust the installation angle of anchors, enabling anchors to control peak shear strength at each level of roof strata and enhance the shear strength of anchors. However, an excessively high pre-tightening force was also an important factor that led to anchor rupture. Liu et al. [10] verified the feasibility of using anchor bolt extension technology that could adapt to the deformation of surrounding rocks and effectively prevent roadway caving triggered by anchor breakage. Wang et al. [11], conducted a shear test on prestressed anchor blocks with structural planes by using a large model test bench; analyzed the tensile, bending,

and shear failure characteristics of anchors; and studied the helical structure of anchors via ABAQUS 2020. Their study results showed that the shear stress of anchors experienced an alternate change process from strong to weak, from weak to strong, and finally, from strong to weak. Tong et al. [12] and Shan et al. [13–18] proposed a combination of anchors and C-shaped canals for conducting double-shear tests. Their results proved that anchors and C-shaped canals could improve the transverse shear capacity of supporting materials during the shear process and strengthen the axial ultimate bearing capacity of anchors. He et al. [19], Yang et al. [20], Ming et al. [21], and Tao et al. [22] studied the mechanical and supporting characteristics of anchors with negative Poisson's ratio (NPR) through field investigation and numerical simulation. Aziz et al. [23] conducted a single-shear test of full-wrapping-type anchors and determined that the shear strength of spiral and groove-type anchors was lower than that of ordinary anchors and the peak shear load of anchors could be reduced by increasing the pre-tightening load. By conducting double-shear tests, Mirzaghorbanali et al. [24] concluded that the peak shear load of round steel strand anchors was higher than those of indented and spiral steel strand anchors. Li et al. [25] believed that the key to the stability of surrounding rocks in a roadway with a soft rock composite roof lay in reasonably arranging anchors and elevating their effective stress diffusion efficiency. This author explored the influence of different anchor supporting parameters on the stress diffusion of surrounding rocks through numerical simulation software and proposed the optimal parameters. Wang et al. [26] believed that tensile load presented a cubic polynomial relationship with torque and essentially exhibited linear relationships in different stages. The failure mechanism of the anchorage section was manifested by initial tensile failure, followed by shear failure. The drawing–torque–displacement relations of anchors experienced three stages: loading, softening, and residual. Tang et al. [27] designed and developed an energy-absorbing damping anchor bolt that consisted of the bolt body, tray, constant-resistance energy absorption device, and specially shaped bolt nut; energy absorption and support could not only effectively guide and control the release and transformation of impact energy but also consume impact energy in the cushioning process of anchor bolts, ensuring the stability of surrounding rocks and the supporting protection system. Aziz et al. [28] performed shear tests on seven steel strand anchors (diameter: 15.2 mm) at angles of 0°, 30°, and 45°, and believed that the stiffness of sheared anchors could be improved by increasing the shear angle. Wang et al. [29] reported that anchors would experience pitting corrosion due to the long-term action of O, Cl, and S in the surrounding rock environment, reducing the outer diameter and bearing capacity of anchors and finally leading to their rupture.

Faham Tahmasebinia1 et al. [30] established the static and dynamic loading numerical model of double shear test in ABAQus/Explicit. Through static tests and dynamic tests, the effects of bolt diameter, steel yield strength and ultimate strength, dynamic load speed, and dynamic load mass on bolt displacement, shear force, and energy dissipation capacity were studied.

The aforementioned studies focused on the influencing factors of the spiral structure and tensile–shear mechanical properties of anchors, in which the fracture and ejection formulas of the whole anchor with empirical constants have been deduced. Moreover, the mechanical properties of anchors have been verified to be improved by the C-shaped canal–anchor combination, NPR anchors, and spiral- and groove-type anchors. However, the dynamic evolution mechanisms of anchor wire breaking and ejection and the energy gathering and dissipation of protective devices have not been comprehensively studied. Considering the unpredictability of anchor incidents, this study is based on the approach of single-axis tension tests to infer cables' dynamics and evaluate protection device performance. Field tests in Zhangji Mine corroborated laboratory findings, offering valuable insights for understanding cable pull-out dynamics and protection device design.

2. Analysis of Tensile Test in Anchor Cables and Evaluation of Ejection Kinetics

Utilizing the energy conservation principle, the stress–strain data derived from tensile tests on anchor cables were integrated to obtain the strain energy density at various stages of the cable's tension. In context of the cable pull-out incident in the 1632 (3) roadway of Pan San Mine, both the ejection kinetic energy and speed were calculated through the strain energy density observed during unloading. This analysis provides data for the design of protection devices.

2.1. Tensile Test of Cable Steel Wire

Anchors (1860 MPa, 21.8 mm in diameter) were selected and cored to prepare specimens with a diameter of 6 mm and a length of 0.2 m. The stress–strain curves of anchor wires were acquired through a tensile test, as shown in Figure 1.

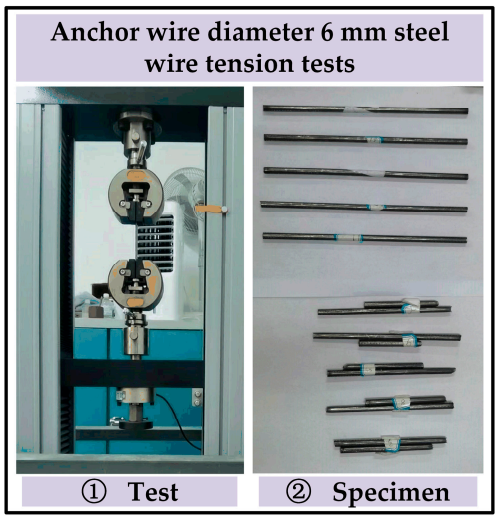


Figure 1. Tensile test diagram of anchor steel wires.

In this test, 20 anchor wire specimens were used and tested with a W-type universal tensile machine. The test data were averaged and plotted. The stress–strain curves of the anchor steel wires are presented in Figure 2.

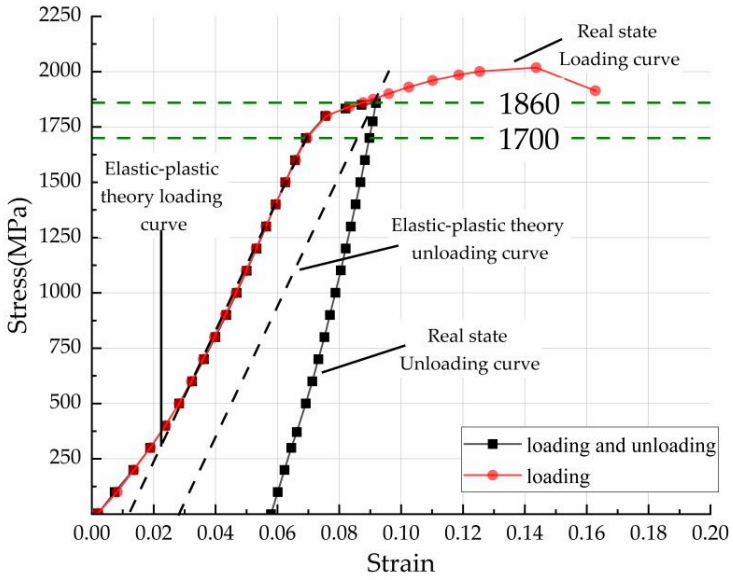


Figure 2. Stress–strain curves of anchor steel wires.

The following data can be obtained through the stress–strain curves.
Strain energy density in the elastic loading stage:

$$U_t = \int_{0.01216}^{0.06919} f(x_1)\mathrm{d}x_1 = 58.65\mathrm{e}^6\mathrm{J}/m^3 \quad (1)$$

Strain energy density in the plastic loading stage:

$$U_\mathrm{s} = \int_{0.06919}^{0.09184} f(x_2)\mathrm{d}x_2 = 33.3038\mathrm{e}^6\mathrm{J}/\mathrm{m}^3 \quad (2)$$

Strain energy density in the unloading stage:

$$U_x = \int_{0.05789}^{0.09079} f(x_3)\mathrm{d}x_3 = 27.528\mathrm{e}^6\mathrm{J}/m^3 \quad (3)$$

Dissipated energy density in the loading/unloading stages:

$$U_h = U_t + U_s - U_x = 64.4258\mathrm{e}^6\mathrm{J}/m^3 \quad (4)$$

In the preceding formulas, U_t is the strain energy density in the elastic loading stage, U_s is the strain energy density in the plastic-elastic loading stage, U_x denotes the strain energy density in the unloading stage, U_h represents the dissipated energy density in the loading/unloading stage, $f(x_1)$ is the stress–strain curve in the elastic stage, $f(x_2)$ is the stress–strain curve of the plastic stage, and $f(x_3)$ is the stress–strain curve in the unloading stage.

Anchor wire breaking and ejection conform to theorem of conservation of energy, as follows:

$$\frac{1}{2}mv_1^2 = W_x \quad (5)$$

Stored total strain energy in anchor wire breaking:

$$W_x = U_x\pi r^2 L \quad (6)$$

Partial stored strain energy in anchor wire breaking:

$$W_{\mathrm{d}x} = U_x\pi r^2 L_1 = W_x\frac{L_1}{L} \quad (7)$$

In the preceding formulas, W_x is the stored total strain energy in anchor wires, $W_{\mathrm{d}x}$ represents the partial stored strain energy in anchor wire breaking, v_1 is the ejection speed, m stands for the anchor wire breaking mass, L is the total tensile elongation of anchor wires, and L_1 is the anchor wire breaking length.

2.2. Case Analysis of Anchor Wire Breaking and Ejection

Based on the strain energy density of the anchor wire in the unloading stage, combined with the on-site data, the kinetic energy and velocity at the time of anchor breakage ejection were calculated.

In November 2017, anchor wire breaking occurred at the 1632 (3) roadway in Pansan Mine, with an average buried depth of 600 m and a roadway section of 5.2 m (width) × 3.3 m (height). The roadway was supported by a bolt–mesh–anchor combined system. The anchors were 1860 MPa steel strands with a specification of Φ22 mm × 6.3 m (length). The lithologies of the roadway roof and floor are displayed in Figure 3.

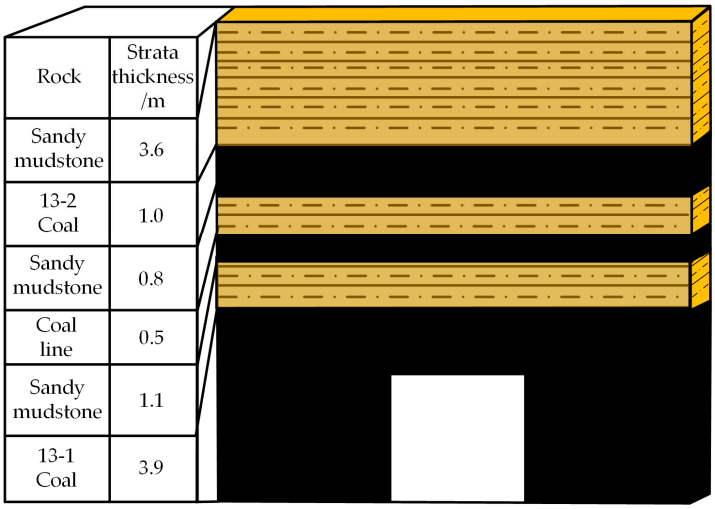


Figure 3. Diagram of the roof lithology of the 1632 (3) roadway.

On the field, the anchor wire breaking and ejection length L_1 was 0.3 m, the length of the anchor end L_2 was 0.2 m, the total anchor length L_3 was 6.3 m, the radius r of anchor wire breaking was 0.003 m, the ejection speed was v_1, and the steel density ρ was 7870 kg/m^3. The locations of L_1, L_2, and L_3 in the Formulas (8)–(10) are shown in Figure 4.

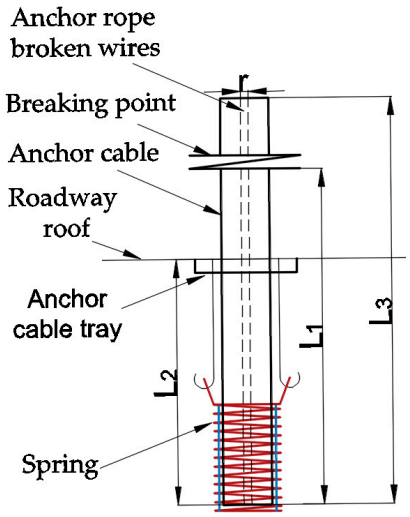


Figure 4. Diagram of the L_1 L_2 L_3 position in the formula.

As shown in Equation (6), the stored total strain energy in anchor wire breaking is expressed as follows:

$$W_x = U_x \pi r^2 (L_3 - L_2) = 4745.44 \text{ J}, \tag{8}$$

From Equation (7), the partial strain energy in anchor wire breaking can be obtained as follows:

$$W_{dx} = W_x \frac{L_1 - L_2}{L_3 - L_2} = 77.79 \text{ J}, \tag{9}$$

From Equation (5), the initial anchor wire breaking and ejection speed is expressed as follows:

$$v_1 = \sqrt{\frac{2W_{dx}}{m}} = \sqrt{\frac{2W_{dx}}{\rho \pi r^2 L_1}} = 48 \text{ m/s}, \tag{10}$$

3. Tensile Test of Spring Protection Devices

Through tensile tests of spring protection devices of varying diameters, the energy absorption capacity was obtained through integrated test results. Leveraging the energy conservation principle and considering the kinetic energy and speed associated with anchor cable pull-out and ejections, an evaluation was undertaken to determine the device's adequacy in meeting engineering specifications.

3.1. Dynamic Impact Assessment of Spring Protection Device through Energy Conversion Analysis

In case of anchor wire breaking and ejection, the ejecting steel wires hit the spring base of the protective device, subjecting the spring to deformation and allowing it to absorb energy and exert a protective effect. The protective device for anchor wire breaking is as shown in Figure 5. During the construction of mine roadway support, a steel chain equipped with hooks or D-shaped buckles at both ends serves as a connecting element. One end of this steel chain is suspended from the roof anchor net, while the other end is linked to the handle of the anchor cable protection device. Detailed implementation measures are depicted in Figure 6.

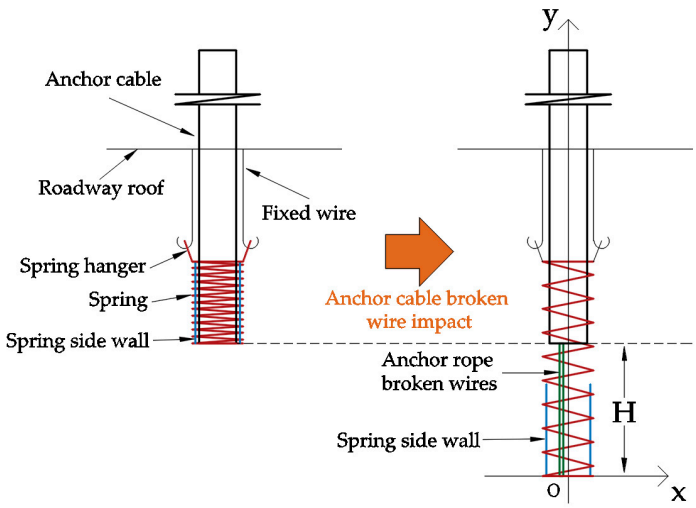


Figure 5. Schematic of impact protection device for anchor wire breaking.

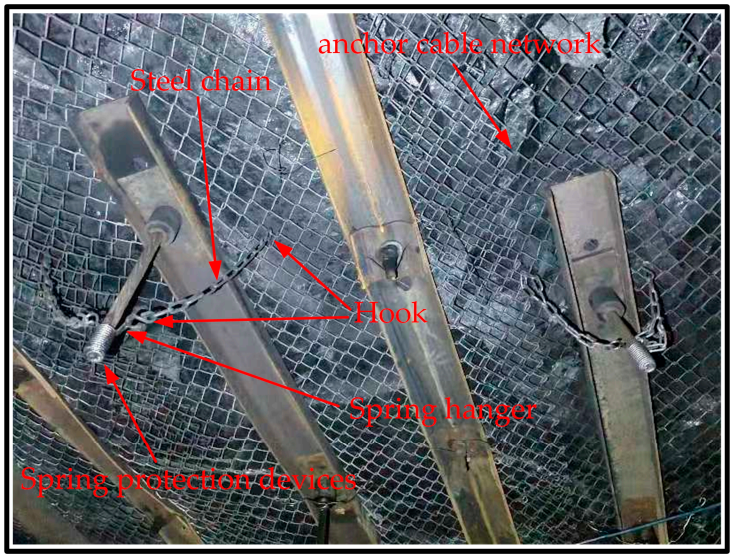


Figure 6. Installation schematic of the anchor protective devices.

The energy that can be absorbed by the protective device is expressed as follows:

$$W = \int_0^H k\mathrm{d}y, \tag{11}$$

The safety criterion for energy conversion between anchor wire breaking and ejection and the protective device is described as follows:

$$W_x = \frac{1}{2}mv_1^2 \leq W = \int_0^H ky\mathrm{d}y, \tag{12}$$

where H is the stretching amount of the spring, k stands for the elastic coefficient of the protective device for anchor wire breaking, and W represents the effectively absorbed energy by the protective device for anchor wire breaking and ejection.

3.2. Tensile Test of Spring Protection Devices

The anchor protective device had two specifications: the protective device with a spring wire diameter of 4 mm and 15 active turns and the protective device with a spring wire diameter of 5 mm and 12 active turns. The diameter of both springs was 22 mm. The relevant parameters of the protective devices were obtained through tensile test, providing a reference basis for further studying protective devices.

Ten protective devices with a spring wire diameter of 4 mm and ten with a spring wire diameter of 5 mm were prepared for the test. The test process was as follows. The "cross bar" of a T-shaped steel was fixed with a spring hanger by using steel wires. The "vertical bar" was held by a gripper on the tensile machine. A hole was drilled onto the spring base for a high-strength long rod screw to pass through. This screw was fixed with bolts. The long rod of the screw was held by the gripper under the tensile machine for the tensile test. The test results were averaged, followed by curve fitting. The tensile loading rate was 50 mm/min. The test process is displayed in Figure 7, the test results of the protective device with a wire diameter of 4 mm are presented in Figure 8, and the test results of the protective device with a wire diameter of 5 mm are presented in Figure 9.

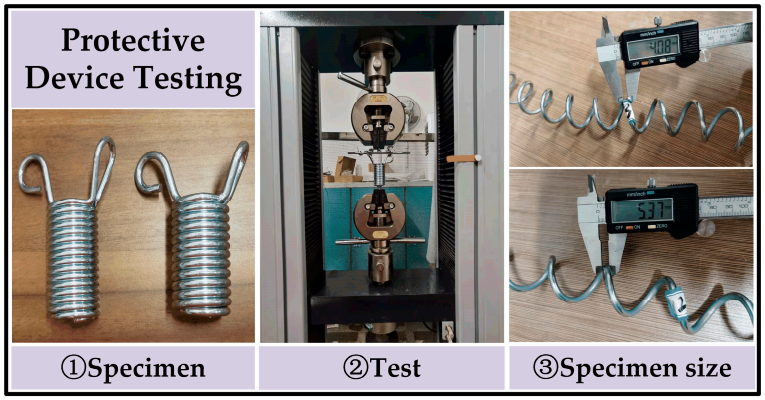


Figure 7. Test flowchart of the protective devices for anchors.

As obtained from the test, 77.7 J of energy was absorbed when the protective device with a spring wire diameter of 4 mm was stretched, while 1092 J of energy was absorbed when it was stretched by 0.83 m. In addition, 1424 J of energy was absorbed in case of ultimate stretching by 1.03 m.

For the protective device with a spring wire diameter of 5 mm, 77.7 J of energy was absorbed when it was stretched by 0.1 m, while 1308 J of energy was absorbed in case of ultimate stretching by 0.83 m.

In summary, both protective devices can bear the impact kinetic energy of anchor wire breaking and ejection. The energy absorption efficiency of the protective device with a

spring wire diameter of 5 mm was superior to that of the protective device with a spring wire diameter of 4 mm. However, the ultimate energy absorption capacity of the former was smaller than that of the latter.

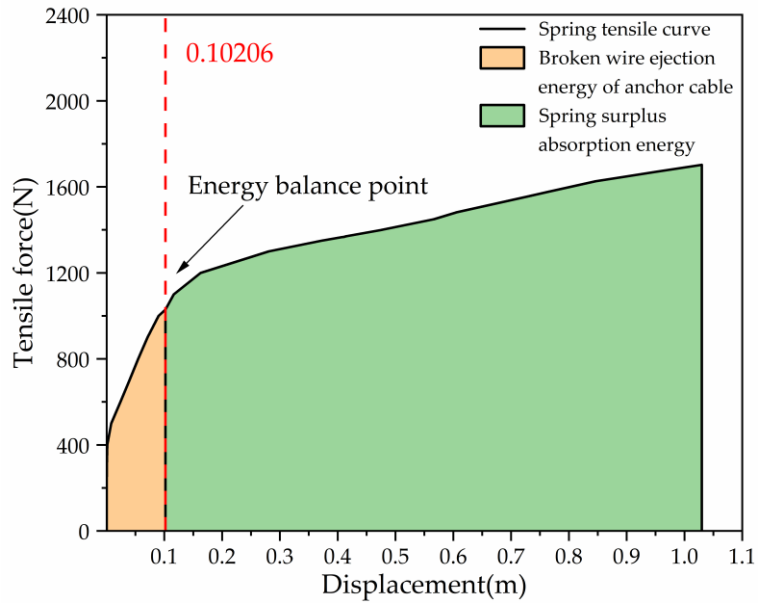


Figure 8. Force–displacement curves of the protective devices with a wire diameter of 4 mm.

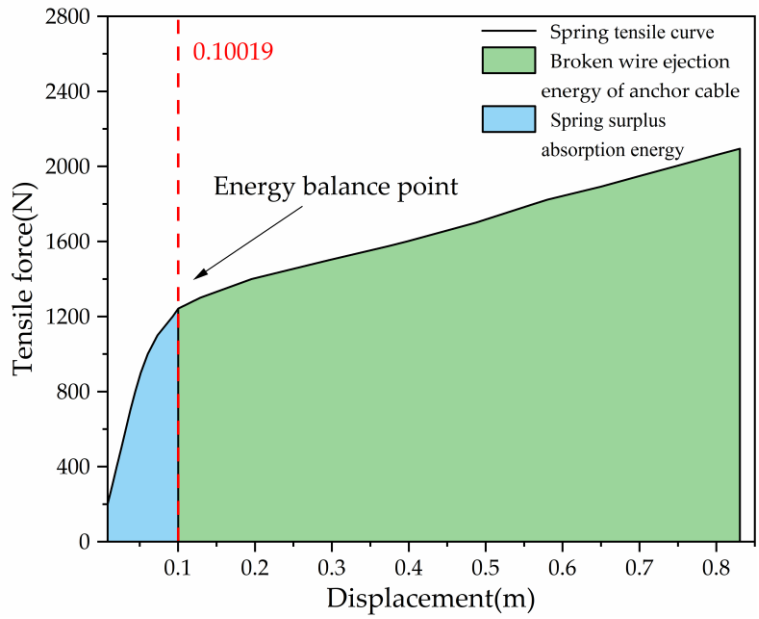


Figure 9. Force–displacement curves of the protective devices with a wire diameter of 5 mm.

4. Numerical Simulation of Impact Protective Devices for Anchor Wire Breaking

Due to the limitations of tensile tests on protection devices and the absence of dynamic impact verification, dynamic simulations of the anchor cable protection device were executed using ANSYS Workbench software.

Initially, the model was constructed utilizing Rhino software and subsequently imported into ANSYS Workbench software. The model comprised a total of 50,772 units and 25,396 nodes. The explicit dynamics module was employed to solve the model. Contrasting with the tensile test in Section 3, which involves static load tension, ANSYS Workbench software simulates the impact of dynamic loading. Given that dynamic loading impacts

necessitate superior material strength properties, it is anticipated that the energy absorbed by the spring in the numerical simulation will be less than that in the test.

The protective device of Specification I had a 65 Mn spring with a wire diameter of 4 mm and 16 turns. The protective device of Specification II had a 65 Mn spring with a wire diameter of 5 mm and 13 turns. The other structural materials of the model were structural steel. Considering that 65 Mn conformed to the GB/T61 standard, structural steel was the default material of ANSYS, and the permissible shear stress coefficient of the materials was 0.7 [31]. The boundary conditions were the roof and the fixed supporting points on the roof. Different initial velocities were applied to the cross section of the broken anchor wire above the roof as the load was applied. The length and diameter of anchor wire breaking and ejection were 0.3 m and 6 mm, respectively.

The numerical simulation results are analyzed in accordance with first strength theory and third strength theory to determine whether the anchor cable protection device is damaged. The geometric structure and the load and constraint positions of the anchor cable protection device are shown in Figure 10. The flowchart of the ANSYS Workbench simulation is shown in Figure 11. The material parameters of the anchor cable protection device are provided in Table 1. The technical parameters of the anchor cable protection device are listed in Table 2.

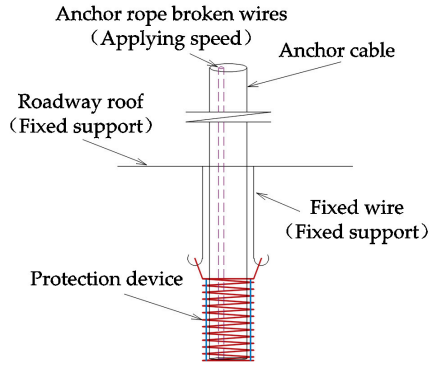


Figure 10. Schematic of the load and constraint positions of the anchor protective devices.

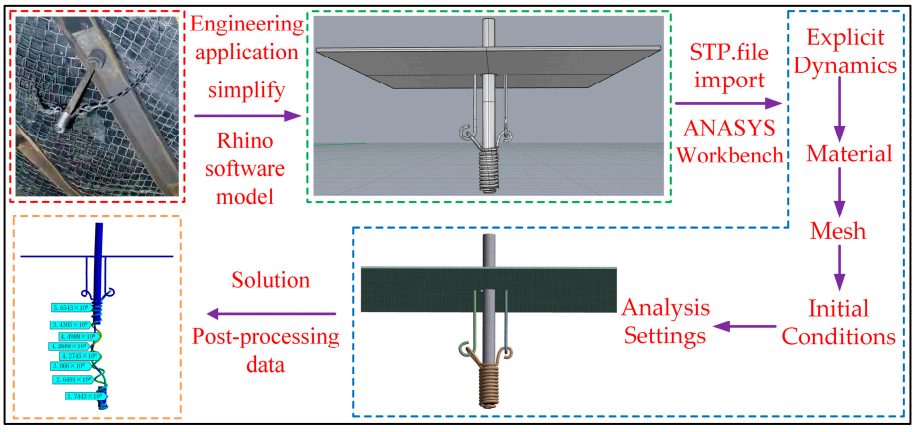


Figure 11. The flowchart of the ANSYS Workbench simulation.

Anchor protective device with Specification I: At an anchor wire breaking and ejection speed of 70 m/s, the maximum principal stress of the protective device is displayed in Figure 12, the maximum shear stress is shown in Figure 13, and the total deformation and equivalent elastic strain are exhibited in Figure 14.

Table 1. Properties of the anchor protective devices and other materials.

Material	Young's Modulus /GPa	Shear Modulus /GPa	Bulk Modulus /m^2	Poisson Ratio	Density /MPa	Tensile Strength/MPa	Yield Strength/MPa	Shear Force and Tensile Force Coefficient	Permissible Shear Stress /MPa
Structural steel	1950	1.86	0.00038	4.5	1.59	460	250	/	/
Mn65	1950	1.86	0.00038	4.5	1.59	980	785	0.7	686

Table 2. Technical parameters of the anchor protective device models.

Wire Diameter of Protective Device /mm	Total Height /mm	Spring Height /mm	Spring Wire Diameter /mm	Total Number of Turns /turns	Protective Wall Height of Spring Base /mm	Thickness of Spring Base /mm
25	100	85	5	13	8	1
25	100	85	5	16	8	1

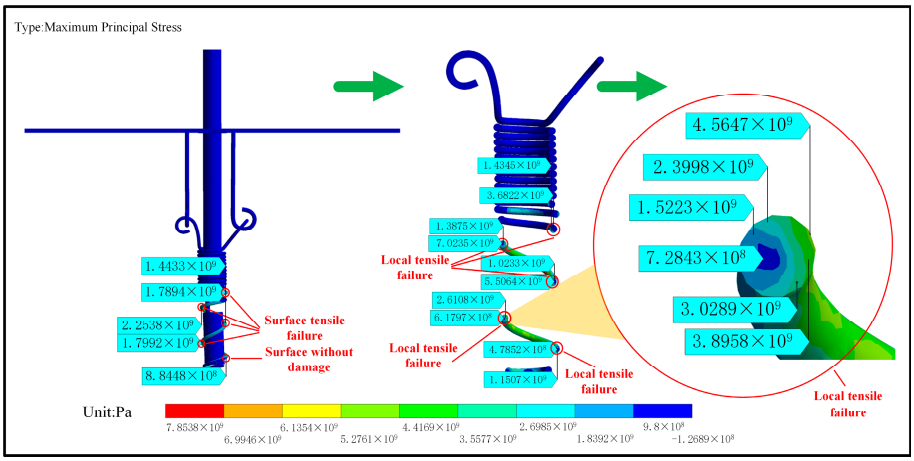


Figure 12. Diagram of the maximum principal stress distribution of the protective device.

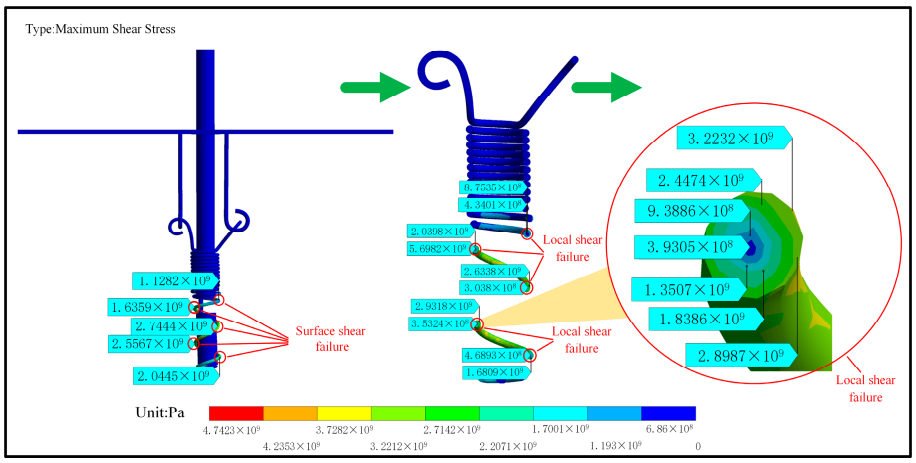


Figure 13. Diagram of the maximum shear force distribution of the protective device.

The ejection energy was 163 J at an anchor wire breaking and ejection speed of 70 m/s. In accordance with first strength theory and combined with Figure 12, stress concentration was determined to occur on the surface of the middle spring section. The peak principal stress was about 2253 MPa, indicating tensile failure, while the local principal stress was 884 MPa, reflecting no failure. The cross section of the spring demonstrated local tensile failure, and stress in the middle section of the spring was distributed in a ring shape, which was small inside and large outside. The principal stress in the center of the cross section was about 728 MPa, and the principal stress in the outer ring was about 4565 MPa. That is, the spring was intact inside, and tensile failure occurred outside. In accordance with third

strength theory and combined with Figure 13, stress concentration was observed to occur on the surface of the middle section of the spring. The maximum shear stress peak value was about 2744 MPa, resulting in shear failure. The cross section of the spring exhibited local shear failure. The stress of the cross section of the spring was distributed in a ring shape. The maximum shear stress at the center of the cross section was about 393 MPa, and the maximum shear stress at the outer ring was about 3223 MPa. That is, the surface of the spring experienced shear failure but remained intact inside. As shown in Figure 14, the maximum elastic strain of the spring was 4.7% and the maximum deformation was 0.076 m. The lower part of the spring of the protective device was deformed considerably, whereas the upper part was hardly deformed.

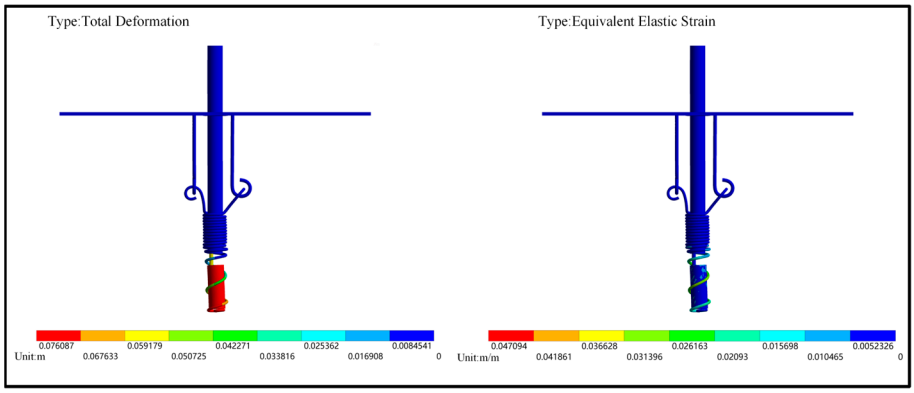


Figure 14. Distribution diagram of total deformation and equivalent elastic deformation.

At an anchor wire breaking and ejection speed of 80 m/s, the maximum principal stress, maximum shear stress, total deformation, and equivalent elastic strain of the protective devices are depicted in Figures 15–17.

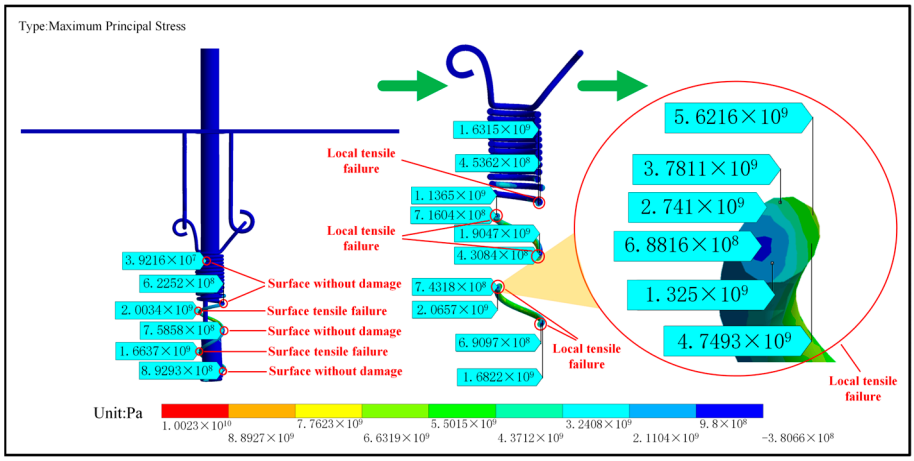


Figure 15. Diagram of the maximum principal stress distribution of the protective device.

The ejection energy was 214 J at an anchor wire breaking and ejection speed of 80 m/s. Combining first strength theory and Figure 15, stress concentration appeared on the surface of the middle spring section, and the peak principal stress was about 2003 MPa, resulting in tensile failure. The principal stress in the middle and upper sections was 622 MPa, indicating no failure. The cross section of the spring exhibited local tensile failure, and the cross-section stress of the spring presented an asymmetric annular distribution, with the central principal stress of the cross section being around 688 MPa and the outer principal stress being approximately 5621 MPa. That is, the inner part of the spring was intact while the outer part underwent tensile failure. In accordance with third strength theory combined

with Figure 16, stress concentration occurred on the surface of the middle spring section. The maximum shear stress was around 2702 MPa, and shear failure occurred. A complete shear failure was generated on the lower segment of the spring section, and local shear failure of the section appeared at other positions. Stress on the spring section exhibited an asymmetric annular distribution, i.e., small inside and large outside. Shear stress at the center of the cross section was about 1142 MPa, while shear stress at the outer ring was approximately 3632 MPa. That is, the inner part of the spring was intact, whereas the outer part was damaged by shear. As shown in Figure 17, the maximum elastic strain of the spring was 6.1% and maximum deformation was 0.087 m. The lower part of the spring of the protective device was deformed considerably, whereas the upper part was hardly deformed.

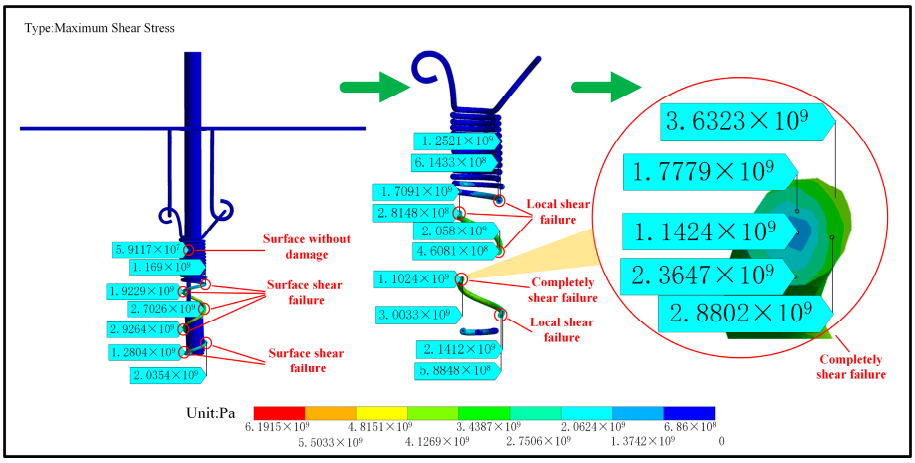


Figure 16. Diagram of the maximum shear force distribution of the protective device.

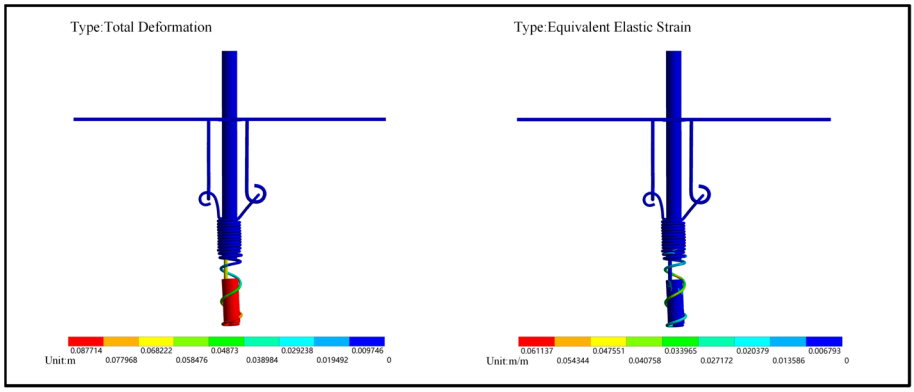


Figure 17. Distribution diagram of total deformation and equivalent elastic deformation.

The limit impact load of the protective device with Specification I was only 70 m/s. The lower part of the spring was rapidly stretched and deformed after being hit, and the diameter was reduced, due to the thin wire diameter of the spring. The inner wall of the spring was locked up upon contact with the outer wall of the anchor end, leading to the tensile failure of the lower part of the spring. The upper part was hardly stretched, significantly weakening the energy absorption performance of the spring, which was considerably less than the energy absorption data measured via the spring tensile test. Increasing the wire diameter of the spring can slow down the stretching speed of the spring and enhance its energy absorption performance during stretching.

Anchor protective device with Specification II: At an anchor wire breaking and ejection speed of 160 m/s, the maximum principal stress of the protective devices is shown in

Figure 18, the maximum shear stress is displayed in Figure 19, and total deformation and equivalent elastic deformation are exhibited in Figure 20.

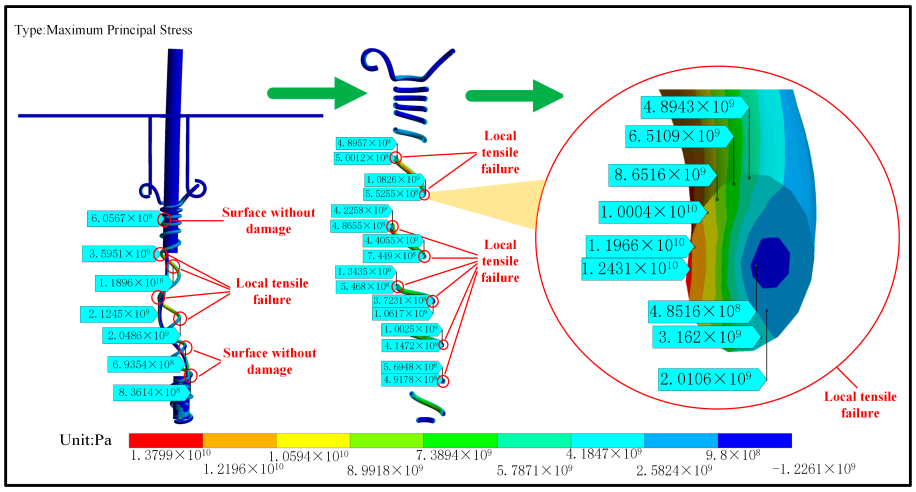


Figure 18. Diagram of the maximum principal stress distribution of the protective device.

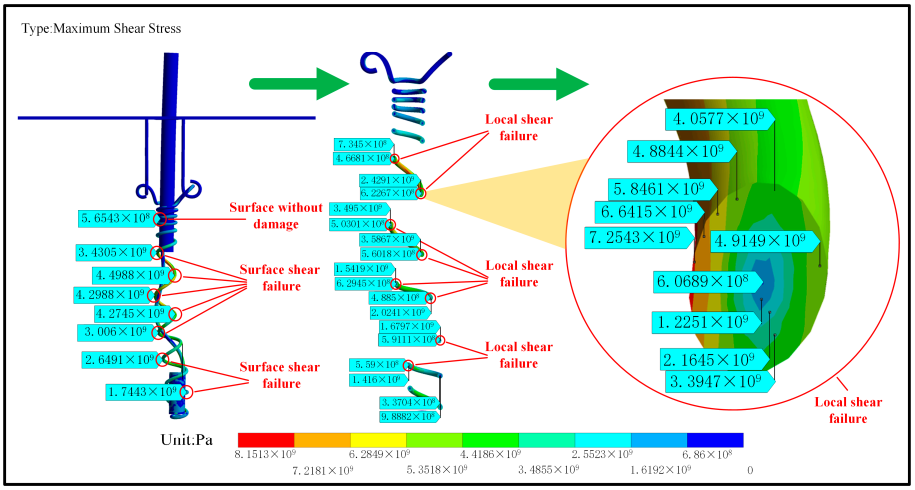


Figure 19. Diagram of the maximum shear force distribution of the protective device.

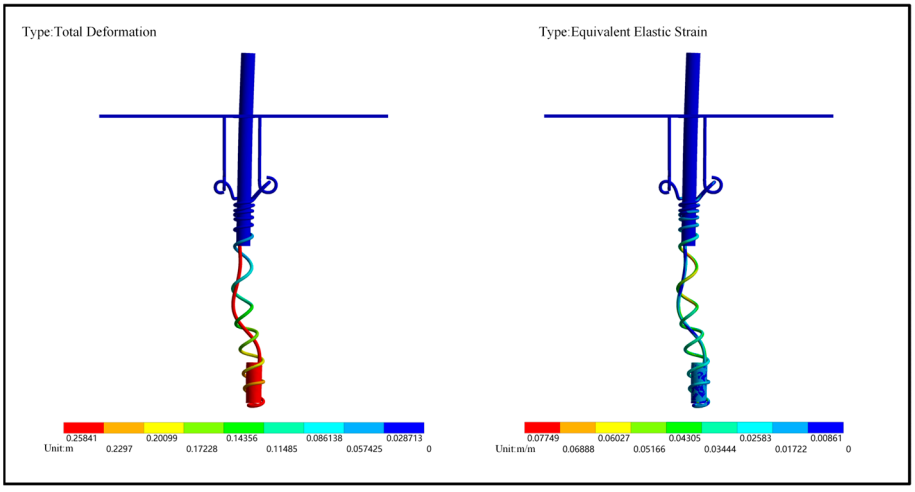


Figure 20. Distribution diagram of total deformation and equivalent elastic deformation.

The ejection energy was 854 J at an anchor wire breaking and ejection speed of 160 m/s. Combining first strength theory and Figure 18, stress concentration appeared on the surface of the middle section of the spring, and the peak principal stress was about 11.89 GPa, resulting in tensile failure. Local principal stress in the middle and lower sections was about 694 MPa, and local principal stress in the middle and upper sections was about 605 MPa, all of which were not damaged. The cross section of the spring exhibited local tensile failure, and stress in the middle and upper sections of the spring presented an asymmetric annular distribution. Principal stress in the center of the cross section was about 485 MPa, and principal stress in the outer ring was around 12.43 GPa. That is, the spring was intact inside while tensile failure occurred outside. In accordance with third strength theory combined with Figure 19, stress concentration occurred on the surface of the middle section of the spring, and the maximum shear stress peak was about 4499 MPa, resulting in shear failure. The cross section of the spring experienced local shear failure, and stress of the spring section was distributed in a ring shape, i.e., small inside and large outside. The maximum shear stress at the center of the cross section was about 606 MPa, and the maximum shear stress at the outer ring was approximately 7254 MPa. That is, the surface of the spring went through shear failure, but it was intact inside. As shown Figure 20, the maximum elastic strain of the spring was about 7.7%, and the maximum deformation was 0.26 m. The middle and lower parts of the spring of the protection device were deformed considerably, while the upper part was not.

At an anchor wire breaking and ejection speed of 170 m/s, the maximum principal stress of the protective device is shown in Figure 21, the maximum shear stress is displayed in Figure 22, and the total deformation and equivalent elastic strain are exhibited in Figure 23.

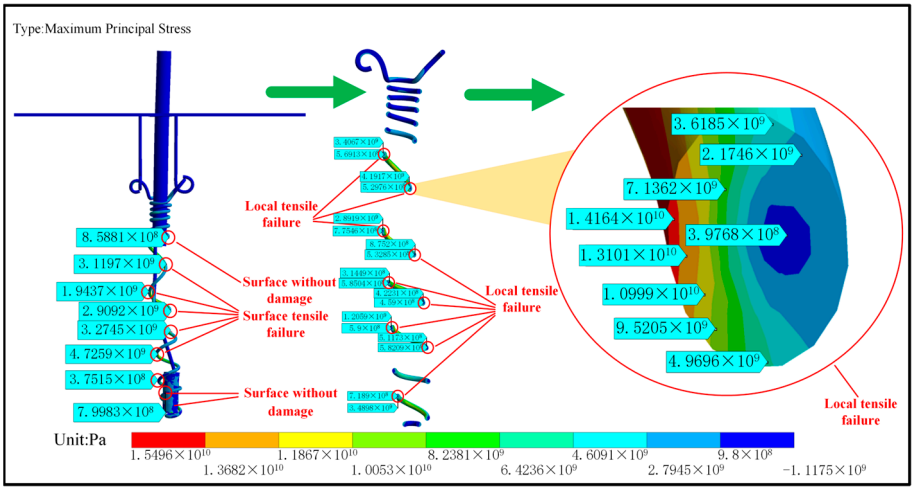


Figure 21. Diagram of the maximum principal stress distribution of the protective device.

Ejection energy was 964 J when the anchor wire breaking and ejection speed was 170 m/s. In accordance with first strength theory combined with Figure 18, stress concentration appeared on the surface of the middle section of the spring, and the peak value of principal stress was about 4726 MPa, resulting in tensile failure. The local principal stress in the lower section was around 375 MPa, and local principal stress in the upper section was approximately 859 MPa, all of which were not damaged. The middle and upper section of the spring went through local tensile failure, and stress in the middle and upper sections of the spring presented an asymmetric annular distribution. Principal stress at the center of the section was about 398 Pa, while principal stress at the outer ring was approximately 14.16 GPa. That is, the spring was intact inside but tensile failure occurred outside. In accordance with third strength theory combined with Figure 19, stress concentration occurred on the surface of the middle and lower sections of the spring, and the maximum value

of the peak shear stress was about 4330 MPa, resulting in shear failure. The middle and lower sections of the spring experienced local shear failure, while the upper and middle sections displayed complete shear failure. At complete shear failure, the cross-section stress of the spring presented an asymmetric annular distribution. The maximum shear stress at the center of the cross section was about 891 MPa, and the maximum shear stress at the outer ring was around 8190 MPa. As shown in Figure 20, the maximum elastic strain of the spring was approximately 11.4%, and maximum deformation was 0.27 m. The middle and lower parts of the spring of the protective device were deformed considerably, while the upper part was not.

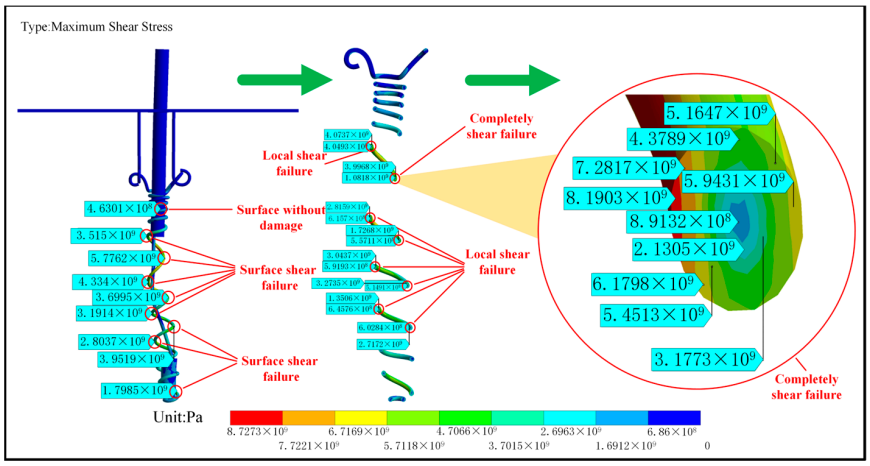


Figure 22. Diagram of the maximum shear force distribution of the protective device.

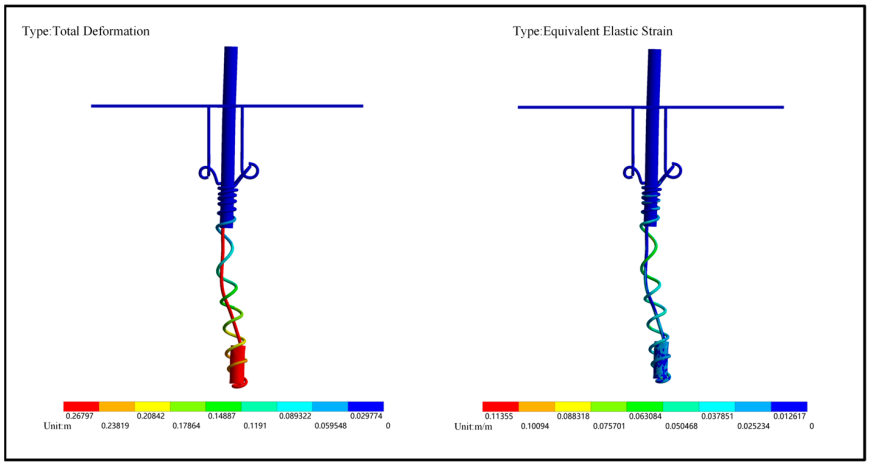


Figure 23. Distribution diagram of total deformation and equivalent elastic deformation.

The ultimate impact load of the anchor protective device with Specification II was 160 m/s, which was considerably higher than the anchor protective device with a wire breaking and ejection speed of 48 m/s. As the spring wire diameter of the protective device increased from 4 mm to 5 mm, the elastic coefficient of the spring was improved. After the protective device was hit, the large deformation of the lower part of the spring was improved, and the middle part of the spring was not locked up with the anchor end, avoiding stress concentration in the lower part of the spring that will result in failure. The tensile deformation of the middle section of the spring absorbed a large amount of impact kinetic energy, which increased the ultimate impact load of the protection device from 70 m/s to 160 m/s, meeting the protection requirements for anchor wire breaking and ejection. However, the upper section of the spring was still locked up upon contact with the anchor end, limiting the energy absorption effect of the spring. In summary, spring texture

can be improved or spring wire diameter can be increased to improve its elastic coefficient further. In addition, spring diameter and spacing between the spring and the anchor can be increased to prevent the upper spring section from being locked up upon contact with the anchor, further improving the energy absorption effect of protective devices.

Findings from the research indicate that the protection efficacy of the 5 mm diameter spring device surpasses that of its 4 mm counterpart.

5. Engineering Application

Informed by the aforementioned studies, the 5 mm diameter spring protection device was selected for large-scale production and subsequently implemented in the 1511 (1) headentry roof anchor tests in Zhangji Mine. The roadway was supported by a network of anchor cables. Each anchor cable, a high-strength prestressed steel strand, measured $\varphi 22 \times 6300$ mm, with a spacing of 1250 mm and row spacing of 900 mm. The anchor bolt, made of screw steel, had dimensions of $\varphi 20 \times 2500$ mm, a spacing of 900 mm, and row spacing of 750 mm. A dedicated individual from the mine was assigned to routinely monitor the anchor cable and measure the tensile deformation produced by the protective device using a steel tape. The protective devices for engineering application are as shown in Figure 24.

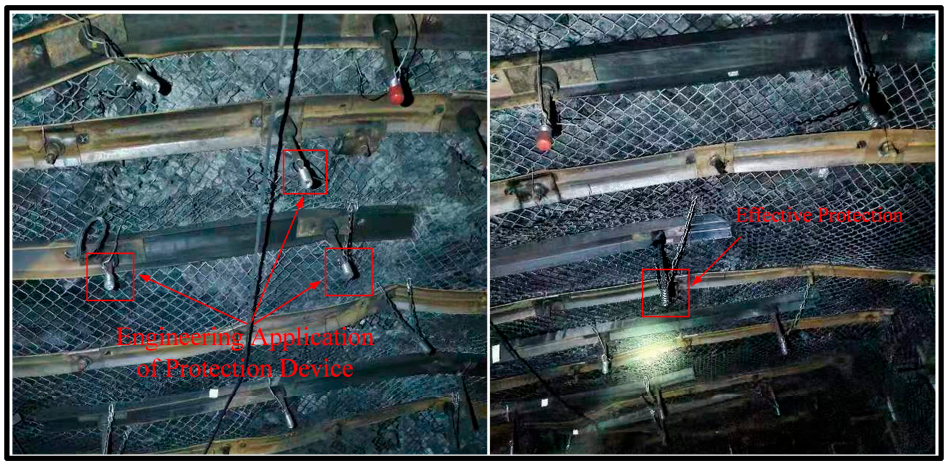


Figure 24. Engineering application of spring protection devices.

Notably, the average roof displacement registered was 31 mm, and only a single incident of anchor cable pull-out and ejection was recorded. Crucially, the cable remained contained through the spring protection device, underscoring its practical viability.

6. Discussion

The working conditions of anchor cables in coal mine roadways present a challenge in observing the ejection speed of a breaking anchor cable wire in the field. This difficulty is also mirrored in the laboratory due to the unique hinged structure of the anchor wire. To overcome this, Section 2 cleverly utilizes the strain energy density of the anchor cable wire during the unloading stage to accurately determine the maximum strain energy and the initial speed at which maximum breakage ejection occurs. This research forms the basis for the development of an anchor cable protective device. In Section 3, a tensile test of the protective device is conducted to ascertain its energy absorption limit under static load conditions, relative to the breaking ejection speed of the anchor cable. This test serves as a mechanical performance parameter for the protective device and sets the stage for a numerical simulation study under dynamic load conditions, such as when an anchor cable breaks and ejects. Numerical simulation, with its advantages of strong intuitiveness, high repeatability, and low cost, is employed in Section 4; the stress and deformation data for the protective device under varying speeds of the anchor wire can be obtained intuitively

by using ANSYS Workbench simulation. These results provide pertinent parameters for experimental design under laboratory conditions, thereby accelerating research progress. Section 5 introduces the application of the protective device in coal mine roadway anchor cable support and verifies its effectiveness. During field application, potential defects in the protective device can be identified for further optimization and improvement. The findings from this research offer valuable insights into the ejection and protection of anchor wires.

7. Conclusions

By exploring the kinetic energy of anchor wire breaking and ejection, the following conclusions were drawn.

1. In accordance with the tensile test of anchor wires and the case analysis of anchor wire breaking and ejection, the strain energy density of anchor wire breaking and ejection was 27.528×10^6 J/m^3, the breaking and ejection speed of the anchor wire that was 0.3 m in length was 48 m/s, and anchor wire breaking length was directly proportional to strain energy but inversely proportional to ejection speed.
2. The tensile test of protective devices indicated that in case of the ultimate stretching of a protective device with a spring wire diameter of 4 mm by 1.03 m, the absorbable energy was 1424 J. The absorbable energy was 1308 J in the event of the ultimate stretching of a protective device with a spring wire diameter of 5 mm by 0.83 m.
3. As revealed in the numerical simulation through ANSYS, after the protective device with a spring wire diameter of 4 mm was hit, the middle section of the spring was locked up upon contact with the anchor end, failing to provide full play to spring performance. After the protective device with a spring wire diameter of 5 mm was hit, the middle section of the spring did not experience tightening or did not get stuck, the effective elongation of the spring increased, and the ultimate impact load increased from 70 m/s to 160 m/s, meeting the field protection requirements.
4. The performance of protective devices can be further improved by increasing the elastic coefficient and diameter of the spring in a protective device.
5. The anchor cable protective device proposed in this paper has the characteristics of high safety and recyclability, which can provide an effective solution for the breaking protection of anchor cable wire in mine roadways.

Author Contributions: Conceptualization, F.G.; methodology, M.T.; validation, J.D.; formal analysis, F.G.; investigation, F.G.; resources, F.G.; writing—original draft preparation, F.G.; writing—review and editing, M.T.; supervision, M.T.; project administration, M.T.; funding acquisition, M.T. All authors have read and agreed to the published version of the manuscript.

Funding: This research was funded by the Anhui Collaborative University Innovation Project (GXXT-2020-056) and the National Natural Science Foundation of China (52074008).

Institutional Review Board Statement: Not applicable.

Informed Consent Statement: Not applicable.

Data Availability Statement: The data that support the findings of this study are available from the corresponding author upon reasonable request.

Conflicts of Interest: The authors declare no conflict of interest.

References

1. Gu, K. The Research on Mechanism of Broken Anchor Wire in Roadway and Protective Measures of the Ejection. Master's Thesis, Taiyuan University of Technology, Taiyuan, China, 2015.
2. Zheng, H.B.; Zhang, Z.Q.; Gu, K. Study on ejection and breaking mechanism of anchor cable and protection schemes. *Saf. Coal Mines* **2016**, *47*, 72–75.
3. He, M.Q. Mechanical Mechanism of Interaction between Grouting Anchor Cable and Surrounding Rock Considering Tension Shear Composite Fracture Effect. Master's Thesis, China University of Mining and Technology, Xuzhou, China, 2021.
4. Yang, R.S.; Li, Y.L.; Wang, M.S.; Zhu, Y.; Cheng, Y.X.; Xiao, C.L.; Zhao, Y. Experimental study of shear mechanical properties of prestressed cable bolts. *J. China Univ. Min. Technol* **2018**, *47*, 1166–1174.

5. Deng, L. Anchor Cable Breaking Mechanism and Control Technology of Composite Roof in Goaf under Near Coal Seam Goaf. Master's Thesis, China University of Mining and Technology, Xuzhou, China, 2021.
6. Niu, F.T. Fracture Mechanism of Composite Layered Roof Anchor Cable in Deep Mining and Surrounding Rock Stability Control. Master's Thesis, Taiyuan University of Technology, Taiyuan, China, 2022.
7. Niu, F.T.; Gong, P.L.; Su, C.; Shi, M.J.; Fan, D.X.; Tian, Y.; Zhang, H. Study on control effect and simulation of anchor cable angle on roof shear dislocation. *Coal Technol.* **2022**, *41*, 39–43.
8. Wang, M.; Xiao, T.Q.; Gao, J.; Liu, J.L. Deformation mechanism and control technology for semi coal and rock roadway with structural plane under shearing force. *J. Min. Saf. Eng.* **2017**, *34*, 527–534.
9. Liu, J.H.; Sun, H.; Zhang, Z.G.; Mao, H.K.; Xu, B.; Gao, L.S. Research on macro-mechanics mechanism of bolt fracturing and its control with high pre-tensioned force. *Coal Sci. Technol.* **2019**, *47*, 91–96.
10. Liu, H.T.; Wang, F.; Wang, G.H.; Zhao, X.D.; Tang, D.; Yu, M.J. Research on lengthening bolt roof support system performance in largely deformed roadway. *J. China Coal Soc.* **2014**, *39*, 600–607.
11. Wang, K.Z.; Zhao, Y.F.; Hu, Z.G.; Nie, Y. Shear test of pre-stressed anchor block and fracture mechanism analysis of anchor cable. *Rock Mech. Rock Eng.* **2022**, *56*, 589–601. [CrossRef]
12. Tong, X.; Shan, R.L.; Liu, N.; Liu, D.; Wei, Y.H. Experimental study on the shear performance of an anchor cable with a C-shaped tube anchored flat structural plane. *Sci. Rep.* **2023**, *13*, 797. [CrossRef]
13. Shan, R.L.; Liang, C.; Liu, W.J.; Jiang, Y.Z.; Li, T.W. Development and application of equipment for anchor cable with c-shaped tube tension-shear test system. *Geofluids* **2022**, *2022*, 5942109. [CrossRef]
14. Shan, R.L.; Liu, W.J.; Li, G.Z.; Liang, C.; Shi, S.G.; Chen, Y.; Zhang, S.P. experimental study on the shear mechanical properties of anchor cable with C-shaped tube. *Sustainability* **2022**, *14*, 9616. [CrossRef]
15. Shan, R.L.; Huang, P.C.; Yuan, H.H.; Meng, C.; Zhang, S.P. Research on the full-section anchor cable and C-shaped tube support system of mining roadway in island coal faces. *J. Asian Archit. Build.* **2021**, *21*, 298–310. [CrossRef]
16. Shan, R.L.; Zhang, S.P.; Xiao, S.C.; Liang, J.Q. Research on anchor cable and C-shaped tube support method in deep layers roadway, experimental study, and numerical simulation. *Shock Vib.* **2021**, *2021*, 7537979. [CrossRef]
17. Shan, R.L.; Bao, Y.S.; Huang, P.C.; Liu, W.J.; Li, G.Z. Study on double-shear test of anchor cable and C-shaped tube. *Shock Vib.* **2021**, *2021*, 9948424. [CrossRef]
18. Shan, R.L.; Tong, X.; Huang, P.C.; Yuan, H.H.; Bao, Y.S.; Liu, N. Research on the anchor cable combined with the c-shaped tube and the mechanical properties. *Rock Soil Mech.* **2022**, *43*, 602–614.
19. He, M.C.; Guo, A.P.; Meng, Z.G.; Pan, Y.F.; Tao, Z.G. Impact and explosion resistance of NPR anchor cable: Field test and numerical simulation. *Undergr. Space* **2023**, *10*, 76–90. [CrossRef]
20. Yang, X.J.; Ming, W.; Gong, W.J.; Pan, Y.F.; He, M.C.; Tao, Z.G. Support characteristics of flexible negative Poisson's ratio anchor cable response to blasting impacts. *Undergr. Space* **2023**, *8*, 162–180. [CrossRef]
21. Ming, W.; Yang, X.J.; Pan, Y.F.; Mao, Y.D.; Wang, X.; He, M.C.; Tao, Z.G. Field test and numerical simulation of initial support effect of negative Poisson's ratio anchor cable under strong impact and vibration. *Tunn. Undergr. Space Technol.* **2023**, *133*, 104955. [CrossRef]
22. Tao, Z.G.; Xu, H.T.; Ren, S.L.; Guo, L.J.; Qin, K.; Zhu, Y.F. Negative Poisson's ratio and peripheral strain of an NPR anchor cable. *J. Mt. Sci.* **2022**, *19*, 2435–2448. [CrossRef]
23. Aziz, N.; Rasekh, H.; Mirzaghorbanali, A.; Yang, G.Y.; Khaleghparast, S.; Nemcik, J. An experimental study on the shear performance of fully encapsulated cable bolts in single shear test. *Rock Mech. Rock Eng.* **2018**, *51*, 2207–2221. [CrossRef]
24. Mirzaghorbanali, A.; Rasekh, H.; Aziz, N.; Yang, G.Y.; Khaleghparast, S.; Nemcik, J. Shear strength properties of cable bolts using a new double shear instrument, experimental study, and numerical simulation. *Tunn. Undergr. Space Technol.* **2017**, *70*, 240–253. [CrossRef]
25. Li, C.; Zhang, W.L.; Huo, T.H.; Yu, R.; Zhao, X.D.; Luo, M. Failure analysis of deep composite roof roadway and support optimization of anchor cable parameters. *Geofluids* **2021**, *2021*, 5610058. [CrossRef]
26. Wang, S.R.; Wang, Y.H.; Gong, J.; Wang, Z.L.; Huang, Q.X.; Kong, F.L. Failure mechanism and constitutive relation for an anchorage segment of an anchor cable under pull-out loading. *Acta Mech.* **2020**, *231*, 3305–3317. [CrossRef]
27. Tang, Z.; Wu, H.; Lv, J.G.; Xin, Z.Z.; Zuo, W.B. Study on mechanical characteristics of energy-absorbing and anti-scour bolts. *Complexity* **2021**, *2021*, 8876517. [CrossRef]
28. Aziz, N.; Mirzaghorbanali, A.; Anzanpour, S.; Rastegarmanesh, A.; Khaleghparat, S.; Nemcik, J.; Oh, J.; Si, G.Y. Angle shear testing of 15.2 mm seven wire cable bolt. *Rock Mech. Rock Eng.* **2022**, *55*, 3919–3937. [CrossRef]
29. Wang, Q.; Wang, F.N.; Ben, A.W.; Peng, R.; Li, J. Corrosion behavior and failure mechanism of prestressed rock bolts (cables) in the underground coal mine. *Adv. Civ. Eng.* **2021**, *2021*, 6686865. [CrossRef]
30. Tahmasebinia, F.; Yang, A.; Feghali, P.; Skrzypkowski, K. A Numerical Investigation to Calculate Ultimate Limit State Capacity of Cable Bolts Subjected to Impact Loading. *Appl. Sci.* **2023**, *13*, 15. [CrossRef]
31. Liu, D.W. The study of the allowable shearing stress of materials. *J. Gansu Sci.* **2008**, *20*, 64–66.

Disclaimer/Publisher's Note: The statements, opinions and data contained in all publications are solely those of the individual author(s) and contributor(s) and not of MDPI and/or the editor(s). MDPI and/or the editor(s) disclaim responsibility for any injury to people or property resulting from any ideas, methods, instructions or products referred to in the content.